Flaw-tolerance in silk fibrils explains strength, extensibility and toughness of spider silk

Melis Arslan[1] and Markus J. Buehler[1,*]

[1] *Laboratory for Atomistic and Molecular Mechanics, Department of Civil and Environmental Engineering, Massachusetts Institute of Technology, 77 Mass. Ave. Room 1-235A&B, Cambridge, MA, 02139, USA*

** Corresponding author, E-mail: mbuehler@MIT.EDU*

ABSTRACT: Silk is an ancient but remarkably strong, extensible and tough material made from simple protein building blocks. Earlier work has shown that the particular molecular geometry of silk with a composite of semi-amorphous and nanocrystalline beta-sheet protein domains provides the structural basis for its characteristic softening-stiffening behavior and remarkable strength at the nanoscale. Yet, an open question remains as to how these nanoscale properties are upscaled so effectively to create strong, extensible and tough silk fibers. Here we discover that the geometric confinement of fibrils to ≈50-100 nm width and arranged in bundles to form larger-scale silk fibers, is the key to explaining the upscaling of the mechanical properties of silk from the atomistic scale upwards. We find that under this geometric confinement, hundreds of thousands of protein domains unfold simultaneously and thereby act synergistically to resist deformation and failure, providing access to enhanced large-scale strength, extensibility and toughness. Moreover, since the material is in a flaw-tolerant state under this geometric confinement, structural inhomogeneities such as cavities or tears that typically act as stress concentrators do not compromise the material performance. Indeed, experimental work showed that the diameter of silk fibrils that make up larger-scale silk fibers are on the order of 20-100 nm, in agreement with our findings. The exploitation of this mechanism in engineering design enables the synthesis of hierarchical fiber materials for superior performance despite limited and inferior building blocks.

Introduction

The great appeal of exploring spider silk, an ancient hierarchical biological protein material (Fig. 1a), lies in its intriguing mechanical properties that emerge despite the material's simple protein building blocks [1-4]. There are many different types of silk with diverse properties. Here we focus specifically on the silk of orb-weaving spiders which is known to be extremely strong, extensible and tough [5-8]. These silk fibers typically feature an initial modulus up to an average of 10 GPa [5, 6, 9], a high extensibility exceeding 50% strain at failure [5, 6, 9-11], which results in toughness values of several times that of Kevlar's [12]. In addition to the relatively large ultimate strength of spider silk in the range from 1-2 GPa [5, 6, 9] and comparable to that of steel, silk features a strength-to-density ratio that is ten times higher than that of steel because of the material's small density (≈1 Mg/m^3).

The mechanical behavior of silk fibers under stretching is highly nonlinear. Beyond an initial high-stiffness regime spider silk softens at the so-called "yield point" where the stress-strain response

gives way to a plateau, eventually leading to an ultimate stiffening regime prior to failure [13]. The combination of these mechanisms results in the characteristic softening-stiffening stress-strain response that is found for many different types of silk [5, 6, 9]. Previous investigations of the mechanical properties of silk have been focused at either the molecular scale [14-17] or at the macroscale [18-20], with some work integrating disparate scales using multiscale models [13]. Earlier work resulted in the elucidation of the specific role of beta-sheet nanocrystals and semi-amorphous regions during deformation of a small nanoscale sample of silk, and was used to extract the mechanical parameters for the constitutive behavior of a single repeat unit of silk [14-16]. In related studies it has also been demonstrated that highly ordered beta-sheet nanocrystals provide strong cross-links between long polypeptide strands that form extended semi-amorphous domains. During deformation, these beta-sheet nanocrystal cross-links facilitate the stretching and unfolding of semi-amorphous domains, to expose their hidden length, by providing a backbone structure [14-16].

What remained puzzling about the results from earlier molecular-level studies of single silk repeat units (≈10 nm) [14-16] is that they showed a remarkable agreement with the larger-scale mechanical behavior of silk (≈several micrometers), despite the stark difference in scale. This includes specifically the observed failure stresses on the order of 1-2 GPa and failure strains in excess of 50% [5]. This raises a fundamental question; how is it possible that the nanoscale mechanical properties can be so effectively upscaled to the larger length-scales seen in silk fibers? This is particularly intriguing given the presence of inhomogeneities such as cavities, surfaces or tears in the material as identified in experimental imaging and analysis, which act as stress concentrators (resembling flaws or cracks). These flaws are expected to compromise the mechanical properties as they serve as seeds for material failure through localized deformation [21-24]. Yet, despite the presence of defects silk displays remarkable mechanical properties at the level of silk fibers with diameters of around 3-4 μm [25, 26] (see Fig. 1a for an overview of scales). This issue calls for a systematic analysis of the mechanisms of deformation, and specifically the role of stress concentrators at varied scales. Directly carrying out full-atomistic analyses, using the same methods as in the studies reported in [14-16], are intractable as they cannot reach the micrometer scales associated with the characteristic dimensions of silk fibers [25, 26]. Macroscale continuum models, on the other hand, are size-scale independent and lack the capacity to describe the material behavior from the bottom-up.

Here we use a coarse-grain mesoscale model as a tool to bridge the dimensional gap and to correlate spider silk's mechanical properties at different scales [27]. The coarse-grain mesoscale model represents the network of semi-amorphous and nanocrystalline domains and is capable of describing length-scales of several micrometers while retaining information about molecular mechanisms (Fig. 1a-b). Resembling the material's physical structure as identified in experimental work [25], each node point reflects a beta-sheet nanocrystal (with dimensions of several ≈nm) and the bonds between nodes correspond to the semi-amorphous regions that connect the crystalline domains. The coarse-grain particle model is implemented in a triangulated network with a particle-to-particle distance of 10 nm (Fig. 1b) and provides a simple model of a silk fibril as shown in Fig. 1d, which is exposed to different boundary conditions that approximate the natural loading of silk fibrils.

The results from atomistic modeling of a single repeat unit of silk (*i.e.*, one beta-sheet nanocrystal embedded in a semi-amorphous domain) [16] are used to determine the constitutive mechanical behavior of the triangulated network as shown in Fig. 1c. The molecular simulations, by establishing a fundamental molecular basis for the formulation of the coarse-grain model, also provide us with a

mechanistic understanding of the origin of the distinct deformation regimes. Figure 1c indicates the different regimes [16] and shows the associated color code used for the field plots depicted in the subsequent figures. Regime I is characterized by a linear-elastic response dominated by homogenous stretching before protein unfolding begins. The transition from Regime I to Regime II is marked by the beginning of the rupture of H-bonds in 3_1-protein helices that make up the semi-amorphous phase, which continues until this entire phase is stretched out. Regime II, governed by the unfolding of the semi-amorphous domains, is the key to the extensibility of silk. Regime III reflects the stiffening behavior that sets in after the exhaustion of unfolding events and the alignment of polypeptide chains. This enables the deformation of beta-sheet nanocrystals that explains the significant stiffening of the material behavior in this regime. Regime IV involves a softening behavior as beta-sheet nanocrystals fail under stick-slip deformation leading to the breakdown of beta-sheet nanocrystal cross-links, and eventual material failure. The mechanical stability of beta-sheet nanocrystals is the key to the ultimate strength of the molecular makeup of silk since they are the last molecular elements that break at the failure point. The importance of the beta-sheet nanocrystal stability and their dependence on the geometry has been discussed in several earlier works, emphasizing that their nanoscale dimension on the order of 2-4 nm is crucial [15, 17].

The atomistically-informed coarse-grain model serves as a tool to address a critical challenge in our understanding of silk, to push chemical concepts to larger scales and to push mechanical concepts to smaller scales (Fig. 1a). It allows us to link the fiber-level mechanical response (at scales of micrometers) with molecular-level mechanisms (at scales of nanometers) that are accessible through our mechanistic understanding of the origin of the distinct deformation regimes in the behavior of silk in Regimes I-IV as described above. Additional details about the model development and motivation, as well as the computational approach used here are provided in the Materials and Methods section.

Results

Because a silk fiber is never perfect and likely contains structural flaws, tears and other imperfections, the issue of microscale mechanical properties of silk rests on the role of these structural inhomogeneities that act as stress concentrators. To implement a stress concentrator as a model for structural inhomogeneities such as cavities [21-24] we consider a system with a single semi-infinite sharp crack that runs along the midline of a microscale slab with dimensions of ≈1.73 μm × 5 μm (representing a fiber with width × length, where the width of the fibril is denoted by H) as shown in Fig. 1b. The overall dimensions resemble the typical geometry of silk fibers with a diameter H on the order of several micrometers, and a length that is several times larger than the width (Fig. 1d).

We begin with an analysis of the deformation field evolution at the edge of the sharp crack, for a microscale sample with dimensions H≈1.73 μm × 5 μm (length kept constant in all cases considered here). We plot the deformation field as an applied tensile (mode I) loading is increased (Fig. 2). The percolation of the molecular deformation mechanisms in the slab is shown in Fig. 2a, combined with the corresponding stress-strain response depicted in Fig. 2b. Different colors in the snapshots correspond to the different molecular-scale mechanisms associated with the regimes described earlier (blue for Regime I, green for Regime II, yellow for Regime III and red for Regime IV; see Fig. 1c). The snapshots shown start from the applied strain where one bond at the edge of the crack reaches the strain associated with transitioning from Regime I to II, at 3% overall strain and at which unfolding of the bonds in the semi-amorphous phase begins. A linear-elastic deformation regime prior to the yielding point (13% strain) is observed (Fig. 2b), and the material eventually fails at strains of less

than 20%. This failure point is much *before* the onset of the characteristic stiffening regime seen in silk stretching experiments, and occurs at much smaller strains than in experimental studies (where failure strains up to 60% are measured) [10, 11, 25].

A detailed analysis of the data shown in Fig. 2a reveals that as the applied strain is increased, the number of bonds that enter Regime II, that is, undergo molecular unfolding of the semi-amorphous phase, increases significantly. The third snapshot Fig. 2a(iii) is significant as it refers to the macroscale strain level at which the overall material response begins to soften (Fig. 2b), marking the yield point. The extension of the region that has entered Regime II at the yield point can be quantified by an effective radius that is estimated to be $r^* = \sqrt{A_{\text{unfold}} / \pi} \approx 110$ nm. This is an important observation that implies that under the presence of stress concentrators there exists a relatively small and finite size region of the material that has entered Regime II, extending over ≈10 silk repeat units in each direction (each of these silk repeat units consists of a semi-amorphous phase and a beta-sheet nanocrystal which are made up of tens of protein strands, as shown in Fig. 1). A further inspection of the deformation field at the yield point shown in Fig. 2a(iii) reveals a small region with an effective radius of ≈17 nm where the molecular bonds have already entered Regime III during which the cross-linking beta-sheet nanocrystals are deformed. It is noted that a very similar behavior as discussed above for tensile (mode I) loading is also seen in shear (mode II) loading, suggesting that this is a general result regardless of the specific loading conditions.

The observation of localization of molecular unfolding for bonds that enter both Regime II and Regime III poses a fundamental question: Is there a characteristic length scale that determines the failure properties of silk at the microscale? Afterall, the analysis of the deformation fields shown in Fig. 2 clearly shows that in a large-scale silk fiber with dimensions of more than a micrometer only a rather small fraction (of less than 1%) of the entire material actually controls its larger-scale mechanical properties while most of the protein domains (more than 99%) do not contribute.

In order to systematically explore if there exists a characteristic length scale that determines the larger-scale failure properties of silk we carry out a series of *in silico* experiments during which we consider samples with decreasing fibril width H while all other parameters are kept constant (including the length of the fibril and the length of the crack which always runs through half the fibril length). We monitor the stress-strain response of each sample and find that as the width H is reduced, the samples reach higher failure stresses and strains as shown in Fig. 3a. We find that the material fails at the strength and the extensibility associated with the deformation of a single repeat unit of silk (*i.e.*, theoretical limit) when the width H is below a critical dimension of H^*≈50 nm. This marks a flaw-tolerant state since the existence of even a very large defect does not compromise the mechanical performance of the fiber. Notably, in addition to matching the results obtained at the molecular scale, the stress-strain curves also agree well with experimental data taken at the fiber scale [10, 11, 25].

To understand the origin of this behavior we compute the area percent of the material that has entered Regime IV (at which beta-sheet nanocrystals fail) and plot this quantity for varied sizes H (Fig. 3b). The analysis shows that indeed, there exists a sudden transition at $H \approx H^*$. Above H^* only a vanishingly small fraction of the material contributes to resisting failure whereas for widths below H^* virtually all the material ahead of the crack contributes to its mechanical properties. We do a similar analysis for the area percent of the material that has entered Regime III and find a transition at H^{**}≈433 nm. At this length scale, however, the material does not display a significant stiffening regime yet and as a result,

shows a much smaller failure stress compared with the theoretical limit (see Fig. 3a). As can be clearly seen from the data, smaller fibril widths H below H^* are needed to exploit the full potential of the material.

Further insight into the link between the molecular level mechanisms and the failure behavior under varied fibril widths is gained by investigating the deformation fields. Fig. 4a-b shows the deformation fields for varied sample widths H for both tension (mode I, Fig. 4a) and shear (mode II, Fig. 4b). While deformation is highly localized to the crack tip region in the largest system considered (H =1.73 μm), and in agreement with the results shown in Figs. 2 and 3, deformation becomes completely delocalized as the system size approaches smaller dimensions below ≈100 nm (Fig. 4a-b, snapshots (ii) and (iii)). This is a significant observation that implies that molecular unfolding of the semi-amorphous phase (Regime II) and the stretching and breaking of beta-sheet nanocrystals (Regimes III-IV) occurs throughout the *entire* sample such that the *entire* material ahead of the defect contributes equally to resisting mechanical failure, providing a concerted action to enhance the strength and extensibility. For example, the concurrent rupture of beta-sheet nanocrystals extends over an area of 50 nm × 2.5 μm. This shows that provided $H \leq H^*$ a very large number of hundreds of thousands of protein domains interact synergistically in defining the mechanical properties of the fibril through a completely percolated network of unfolding protein domains. Reflecting these findings, the dependence of the failure stress on the slab width H follows a non-linear relation as shown in Fig. 4c where the theoretical strength limit is *always* reached for slab widths smaller than H^* despite the presence of defects that act as stress concentrators. We note that both loading conditions, tensile (mode I) and shear (mode II), display the same mechanisms and a similar critical slab length of H^* as is directly shown in Fig. 4c. This observation agrees with fracture mechanics theory [28, 29].

The homogeneous deformation state of silk fibrils is the key to understanding the upscaling mechanisms in spider silk and helps us to quantitatively explain the role of hierarchical structures seen in silk fibers. This pertains in particular to the structures commonly referred to as the "skin-core model" (Fig. 1a and d) [21, 22]. Indeed, earlier experimental work [21, 22, 25, 30] clearly showed that the diameters of silk fibrils that make up larger-scale silk fibers (consisting of bundles of tens to hundreds of so-called silk fibrils making the core of the "skin-core" structure) are on the order of 20-100 nm. We postulate that these silk fibrils, by means of confinement to the critical length-scale below H^*, each reach a homogeneous deformation state. Since silk fibers are relatively small bundles of only tens to hundreds of silk fibrils, they behave similarly as individual silk fibrils and therefore enable silk fibers at larger scales to maintain high strength and extensibility regardless of inhomogeneities that act as stress concentrators. Notably, this concept of forming silk fibers by bundling smaller fibrils resembles the structure splitting mechanism proposed by Ji and Gao [31] for other materials such as bone and nacre. The key idea is to split a larger-scale structure into many small segments, for example through internal surfaces or cracks as illustrated here, and thereby enhance its mechanical properties.

The high strength and high extensibility seen in systems with $H \leq H^*$ result in a high toughness modulus, which is obtained by integrating the stress-strain curve until failure and reflecting the work per unit volume needed to break a material. Several recent experimental studies suggest that silk attains toughness moduli that average to ≈107 MJ/m^3 (across various species) with the largest values exceeding ≈500 MJ/m^3 [5]. The experimental toughness moduli values agree remarkably well with the values calculated from our model that are estimated to be ≈200 MJ/m^3. Our results show that these great toughness moduli are *only* accessible provided that silk fibrils are confined to dimensions below the critical length scale H^* where the extensibility due to Regime II (unfolding plateau) is combined

with the high tensile strength defined by the breaking of beta-sheet nanocrystals in Regime IV. Indeed, our calculations confirm that for larger fibrils with $H>H^*$ (and which are not in the flaw-tolerant regime), the toughness moduli reach only a small fraction of those seen in experimental work. A fibril with width 1.73 μm, for example, reaches a toughness modulus of only 10-20 MJ/m^3, which is in stark contrast to experimental findings (and by a factor of 10 or more too small). This provides evidence for the suggestion that fibrils in natural silk fibers are indeed in a flaw tolerant state, which is quantitatively supported by the experimentally determined geometries.

The emergence of increased structural stability driven by geometric confinement is a recurring pattern that also exists at other scales in the hierarchical makeup of silk. For example, as shown earlier [17] the stability of beta-sheet nanocrystals is greatly enhanced when confined to sizes of 2-4 nm, a finding that also agrees with recent molecular modeling studies [15] and experimental results [25] that suggested a similar length-scale. Our results complement these earlier findings by demonstrating that amongst other molecular-level properties the stability of beta-sheet nanocrystals is made visible at larger micrometer-length scales through the use of bundles of fibrils with H^*=50 nm width each. An overview of various mechanisms at different hierarchical levels is shown in Table 1.

Discussion

The macroscale strength, toughness and extensibility of spider silk fibers originate from the flaw tolerant nature of the constituent fibrils where each fibril fails under a homogeneous deformation state similarly to what is seen in Fig. 4a-b. A critical insight derived from this finding is that molecular unfolding, beta-sheet crystal rupture and other failure mechanisms span the entire structural scale of silk fibrils and up to several micrometer in length given that the width of the fibrils is confined to 50-100 nm (Fig. 4c). This explains why the predictions from molecular simulations [14-16] agreed well with experimental testing of entire silk fibers, because indeed, the molecular properties can be effectively upscaled under geometric confinement such that flaw-tolerance is reached. The nanoscale structure of spider silk is characterized by weak interactions such as H-bonds [14-16], and the hierarchical arrangement of building blocks (Fig. 1a) enhances its material properties so that the larger-scale properties provide a high level of functionality through the synergistic interaction of mechanisms at multiple scales (Table 1). In the case of silk, bundles of tens to hundreds of fibrils, each confined to dimensions of 20-100 nm [21, 22, 25, 30], combine to create a high-performance fiber in which the flaw-tolerant state of each fibril removes the need to create a defect free structure in the first place, and ensures that a massive percolating network of unfolding protein domains emerges that resists deformation and failure.

The appearance of size effects associated with fracture of materials has already been postulated by Griffith in 1920 [28, 29, 32]. The availability of advanced computational and experimental methods make it now possible to quantitatively explore the fracture mechanics of complex hierarchical materials such as spider silk from a bottom-up perspective and to identify critical length scales that define their mechanical properties at various levels, and link these with molecular deformation mechanisms. Griffith stated that the “ideal” molecular level strength is reached as their characteristic size reduces to that of the molecules. Our work shows that the “ideal” strength is reached at scales of around 50 nm, which encompasses hundreds of thousands of protein molecules per fibril that interact synergistically. This shows that the flaw-tolerance length-scale can be rather large provided that the material shows a hierarchical structure. Hierarchical structures in other biological materials have also

been shown to enhance their performance at larger scales (see, for example references [33-39])). In bone, nacre and many other biomaterials, larger-scale mechanisms such as crack bridging, microcracking and others contribute significantly to the overall toughness of the material. It remains an open question whether or not such mechanisms play an important role in silk. These mechanisms could be explored in future work, for example by considering not only individual silk fibrils but bundles of silk fibrils and larger structures.

Methods

Coarse-grain model. As a bridge between the atomistic and the continuum scale we use a mesoscopic coarse-grain model. We implement a simple planar (plane strain) quasi-two-dimensional particle model where the mesh is a triangulated network with a particle-particle distance of $r_0 = 10$ nm and a periodic thickness of $t = 1$ nm (see, Fig. 1b), close to structural data obtained from experimental work by Du *et al*. [25] (where each node points approximates a beta-sheet nanocrystal and the bonds between them represent the semi-amorphous phase). To implement a stress concentrator as a model for inhomogeneities such as cavities [21-24] we consider a system with a single semi-infinite sharp crack that runs along the midline of a microscale slab (dimensions ≈1.73 μm × 5 μm as shown in Fig. 2b, where the width of the slab is varied for different cases studied under constant length of 5 μm as explained in the main text). We deform the slab under both quasi-static tensile (mode I) and shear (mode II) loading to assess the mechanisms under a range of possible boundary conditions (Fig. 1d). The model is not intended to reflect the specific boundary conditions present in silk (which are hard to know *a priori*) but is rather designed to assess fundamental size effects in this material, which we believe is best done in a sufficiently simple model system. This approach has been used successfully in earlier studies [40] and provides fundamental insight into the mechanisms rather than making predictions about specific types of silk.

Model formulation and parameters. A triangulated network model is used to match the nonlinear behavior seen in molecular simulation [14-16] and marked by the four distinct Regimes I-IV: linear-elastic response, unfolding plateau stiffening behavior and finally softening (detailed molecular mechanisms are discussed in the main text). The force-extension behavior for each coarse-grained bond is given by:

$$F_b(\lambda_b) = \begin{cases} k_1 r_0(\lambda_b - 1), & 1 < \lambda_b < \lambda_{b1} \\ k_1 r_0(\lambda_{b1} - 1) + k_{1-2} r_0(\lambda_b - \lambda_{b1}), & \lambda_{b1} < \lambda_b < \lambda_{b2} \\ k_1 r_0(\lambda_{b1} - 1) + k_{1-2} r_0(\lambda_{b2} - \lambda_{b1}) + k_{2-3} r_0(\lambda_b - \lambda_{b2}), & \lambda_{b2} < \lambda_b < \lambda_{b3} \\ k_1 r_0(\lambda_{b1} - 1) + k_{1-2} r_0(\lambda_{b2} - \lambda_{b1}) + k_{2-3} r_0(\lambda_{b3} - \lambda_{b2}) + k_{3-4} r_0(\lambda_b - \lambda_{b3}), & \lambda_{b3} < \lambda_b < \lambda_{b4} \\ 0, & \lambda_b > \lambda_{b4} \end{cases} \quad (1)$$

where λ_{b1}, λ_{b2}, λ_{b3}, λ_{b4} are the transition stretches for each bond. In order to link the constituent transition bond stretches to the macroscopic transition stretches, we fit the initial elastic modulus and transition points using kinematic and constitutive relationships against atomistic data [41]. The transition strains are λ_{b1}=1.10 λ_{b2}=1.35, λ_{b3}=1.45 and λ_{b4}=1.50 and are determined from fitting to

atomistic data [14-16]. Similarly, we fit the initial tensile modulus and determine the initial bond stiffness k_1 accordingly using an expression for the elastic modulus for linear elastic isotropic triangulated networks [41], resulting in $k_1 = 2\left(\sqrt{3}r_0^{\,2}/2\right)E_1 t/3r_0^{\,2} = E_1 t/\sqrt{3} = 0.50$ N/m where the initial modulus is $E_1 \approx 850$ MPa. The bond stiffnesses in different regimes are similarly fit using the ratios of the stiffness changes as identified from molecular modeling [14-16] resulting in $k_{1-2} =$ 0.20 N/m, $k_{2-3} =$ 3.75 N/m and $k_{3-4} =$ 0.3 N/m. The stress-strain behavior of a periodically repeated unit cell of the triangulated network mesh is given in Fig. 1c.

Mechanical loading. We employ an energy minimization approach where for the tensile (mode I) loading cases, 0.3 % strain increments in the *x*-direction is applied as edge displacement followed by an energy minimization carried out using a conjugate gradient algorithm. A maximum of about 70 % strain is applied to the structure until fracture of the entire system occurs. As for the shear (mode II) loading cases, 0.1 % shear strain in the *yx*-direction is applied as edge displacement followed by an energy minimization carried out using the same algorithm. The shear strain is increased until fracture occurs. The stress fields are calculated based on the virial stress [42]. All simulations are carried out using the massively-parallelized LAMMPS code [43]. The study reported here is an exemplification of the use of the multiscale modeling paradigm applied to realistically predict the strength, extensibility and toughness of materials from the molecular scale upwards. The coarse-grain model is a powerful tool to push chemical concepts to larger scales, and to push mechanical concepts to smaller scales as shown in Fig. 1a. It is noted that the boundary conditions of real fibrils are likely different but hard to know in advance. Rather than making assumptions about the loading conditions we decided to focus on the simplest possible ones, the application of displacement loading to resemble mode I and mode II. From a fracture mechanics point of view [28, 29] the setup used here, with only one length-scale *H* in the system (and a slab length >> *H* with a long crack that runs half way through the length), provides a direct way to assess size effects.

Acknowledgements: Support from DOD-MURI, NSF and DOD-PECASE is acknowledged. We acknowledge helpful discussions on silk materials science with David Kaplan (Tufts University) and Joyce Wong (Boston University).

Author contributions: M.A. and M.J.B. conceived and designed the model and computational experiments and associated analysis. M.A. set up, carried out and processed the computational experiments. M.A. and M.J.B. analyzed the data and wrote the paper.

Competing financial interests: The authors declare no competing financial interests.

References

1. Kaplan, D. and American Chemical Society. Division of Polymer Chemistry., *Silk polymers : materials science and biotechnology*. 1994, Washington, D.C.: American Chemical Society. xi,

370 p.
2. Omenetto, F.G. and D.L. Kaplan, *New opportunities for an ancient material.* Science, 2010. **329**(5991): p. 528-31.
3. Vollrath, F., *Spider Silk: Evolution and 400 Million Years of Spinning, Waiting, Snagging, and Mating.* Nature, 2010. **466**(7304): p. 319-319.
4. Rammensee, S., U. Slotta, T. Scheibel, and A.R. Bausch, *Assembly mechanism of recombinant spider silk proteins.* Proceedings Of The National Academy Of Sciences Of The United States Of America, 2008. **105**(18): p. 6590-6595.
5. Agnarsson, I., M. Kuntner, and T.A. Blackledge, *Bioprospecting Finds the Toughest Biological Material: Extraordinary Silk from a Giant Riverine Orb Spider.* Plos One, 2010. **5**(9): p. e11234.
6. Swanson, B.O., S.P. Anderson, C. DiGiovine, R.N. Ross, and J.P. Dorsey, *The evolution of complex biomaterial performance: The case of spider silk.* Integrative and Comparative Biology, 2009. **49**(1): p. 21-31.
7. Dong, Z., R.V. Lewis, and C.R. Middaugh, *Molecular mechanism of spider silk elasticity.* Arch Biochem Biophys, 1991. **284**(1): p. 53-7.
8. Lewis, R.V., *Spider silk: ancient ideas for new biomaterials.* Chem Rev, 2006. **106**(9): p. 3762-74.
9. Swanson, B.O., T.A. Blackledge, J. Beltran, and C.Y. Hayashi, *Variation in the material properties of spider dragline silk across species.* Applied Physics a-Materials Science & Processing, 2006. **82**(2): p. 213-218.
10. Gosline, J.M., M.W. Denny, and M.E. Demont, *Spider Silk as Rubber.* Nature, 1984. **309**(5968): p. 551-552.
11. Vollrath, F. and D.P. Knight, *Liquid crystalline spinning of spider silk.* Nature, 2001. **410**(6828): p. 541-548.
12. Du, N., Z. Yang, X.Y. Liu, Y. Li, and H.Y. Xu, *Structural Origin of the Strain-Hardening of Spider Silk.* Advanced Functional Materials, 2011. **21**(4): p. 772-778.
13. Vollrath, F. and D. Porter, *Spider silk as a model biomaterial.* Applied Physics a-Materials Science & Processing, 2006. **82**(2): p. 205-212.
14. Keten, S. and M.J. Buehler, *Nanostructure and molecular mechanics of spider dragline silk protein assemblies.* Journal Of The Royal Society Interface, 2010. **7**(53): p. 1709-1721.
15. Keten, S., Z.P. Xu, B. Ihle, and M.J. Buehler, *Nanoconfinement controls stiffness, strength and mechanical toughness of beta-sheet crystals in silk.* Nature materials, 2010. **9**(4): p. 359-367.
16. Nova, A., S. Keten, N.M. Pugno, A. Redaelli, and M.J. Buehler, *Molecular and Nanostructural Mechanisms of Deformation, Strength and Toughness of Spider Silk Fibrils.* Nano Letters, 2010. **10**(7): p. 2626-2634.
17. Porter, D. and F. Vollrath, *Nanoscale toughness of spider silk.* Nano Today, 2007. **2**(3): p. 6-6.
18. Becker, N., E. Oroudjev, S. Mutz, J.P. Cleveland, P.K. Hansma, C.Y. Hayashi, D.E. Makarov, and H.G. Hansma, *Molecular nanosprings in spider capture-silk threads.* Nature Materials, 2003. **2**(4): p. 278-283.
19. Zhou, H. and Y. Zhang, *Hierarchical chain model of spider capture silk elasticity.* Phys Rev Lett, 2005. **94**(2): p. 028104.
20. Papadopoulos, P., J. Solter, and F. Kremer, *Hierarchies in the structural organization of spider silk-a quantitative model.* Colloid and Polymer Science, 2009. **287**(2): p. 231-236.
21. Li, S.F.Y., A.J. Mcghie, and S.L. Tang, *New Internal Structure of Spider Dragline Silk Revealed by Atomic-Force Microscopy.* Biophysical Journal, 1994. **66**(4): p. 1209-1212.
22. Vollrath, F., T. Holtet, H.C. Thogersen, and S. Frische, *Structural organization of spider silk.*

Proceedings of the Royal Society of London Series B-Biological Sciences, 1996. **263**(1367): p. 147-151.
23. Frische, S., A.B. Maunsbach, and F. Vollrath, *Elongate cavities and skin-core structure in Nephila spider silk observed by electron microscopy.* Journal of Microscopy-Oxford, 1998. **189**: p. 64-70.
24. Creager, M.S., J.E. Jenkins, L.A. Thagard-Yeaman, A.E. Brooks, J.A. Jones, R.V. Lewis, G.P. Holland, and J.L. Yarger, *Solid-state NMR comparison of various spiders' dragline silk fiber.* Biomacromolecules, 2010. **11**(8): p. 2039-43.
25. Du, N., X.Y. Liu, J. Narayanan, L.A. Li, M.L.M. Lim, and D.Q. Li, *Design of superior spider silk: From nanostructure to mechanical properties.* Biophysical Journal, 2006. **91**(12): p. 4528-4535.
26. Perez-Rigueiro, J., M. Elices, G.R. Plaza, J. Rueda, and G.V. Guinea, *Fracture surfaces and tensile properties of UV-irradiated spider silk fibers.* Journal of Polymer Science Part B-Polymer Physics, 2007. **45**(7): p. 786-793.
27. Buehler, M.J. and Y.C. Yung, *Deformation and failure of protein materials in physiologically extreme conditions and disease.* Nature Materials, 2009. **8**(3): p. 175-188.
28. Anderson, T.L., *Fracture mechanics: Fundamentals and applications*. 1991: CRC Press.
29. Buehler, M.J., H. Yao, H. Gao, and B. Ji, *Cracking and adhesion at small scales: atomistic and continuum studies of flaw tolerant nanostructures.* Model. Sim. Mat. Science and Engr., 2006. **14**: p. 799-816.
30. Augsten, K., P. Muhlig, and C. Herrmann, *Glycoproteins and skin-core structure in Nephila clavipes spider silk observed by light and electron microscopy.* Scanning, 2000. **22**(1): p. 12-5.
31. Ji, B., *A study of the interface strength between protein and mineral in biological materials.* J Biomech, 2008. **41**(2): p. 259-66.
32. Griffith, A.A., *The phenomenon of rupture and flows in solids.* Phil. Trans. Roy. Soc. A, 1920. **221**: p. 163-198.
33. Gao, H., B. Ji, I.L. Jäger, E. Arzt, and P. Fratzl, *Materials become insensitive to flaws at nanoscale: Lessons from nature.* P. Natl. Acad. Sci. USA, 2003. **100**(10): p. 5597-5600.
34. Gao, H.J. and B.H. Ji, *Modeling fracture in nanomaterials via a virtual internal bond method.* Engineering Fracture Mechanics, 2003. **70**(14): p. 1777-1791.
35. Gao, H.J. and S.H. Chen, *Flaw tolerance in a thin strip under tension.* Journal Of Applied Mechanics-Transactions Of The Asme, 2005. **72**(5): p. 732-737.
36. Chou, T.-W., *Microstructural design of fiber composites*. 1992, Cambridge ; New York: Cambridge University Press. xx, 569 p.
37. Espinosa, H.D., J.E. Rim, F. Barthelat, and M.J. Buehler, *Merger of structure and material in nacre and bone - Perspectives on de novo biomimetic materials.* Progress in Materials Science, 2009. **54**(8): p. 1059-1100.
38. Fratzl, P. and R. Weinkamer, *Nature's hierarchical materials.* Progress in Materials Science, 2007. **52**: p. 1263-1334.
39. Bosia, F., M.J. Buehler, and N.M. Pugno, *Hierarchical simulations for the design of supertough nanofibers inspired by spider silk (vol 82, 056103, 2010).* Physical Review E, 2010. **82**(5): p. 056103 (7).
40. Buehler, M.J. and H. Gao, *Dynamical fracture instabilities due to local hyperelasticity at crack tips.* Nature, 2006. **439**(7074): p. 307-10.
41. Arslan, M. and M.C. Boyce, *Constitutive modeling of the finite deformation behavior of membranes possessing a triangulated network microstructure.* Journal of Applied Mechanics-Transactions of the Asme, 2006. **73**(4): p. 536-543.

42. Tsai, D.H., *Virial theorem and stress calculation in molecular-dynamics.* J. of Chemical Physics, 1979. **70**(3): p. 1375-1382.
43. Plimpton, S., *Fast parallel algorithms for short-range molecular-dynamics.* Journal of Computational Physics, 1995. **117**: p. 1-19.
44. Keten, S. and M.J. Buehler, *Geometric confinement governs the rupture strength of H-bond assemblies at a critical length scale.* Nano Letters, 2008. **8**(2): p. 743-748.
45. Cranford, S.W., Tarakanova, A., Pugno, N., Buehler, M. J., *Nonlinear constitutive behaviour of spider silk minimizes damage and begets web robustness from the molecules up.* in submission.
46. Poza, P., J. Perez-Rigueiro, M. Elices, and J. Llorca, *Fractographic analysis of silkworm and spider silk.* Engineering Fracture Mechanics, 2002. **69**(9): p. 1035-1048.

Table and table caption

Table 1 | Summary of key structures and associated mechanisms of upscaling from the atomistic to larger scales (see also Fig. 1a for an overview of structural levels in spider silk).

Structural detail	Scale/level	Mechanism
Beta-strand	Angstrom-nanometer	Critical beta-strand length for heightened stability of H-bond clusters; cooperativity of H-bonds maximized at a critical scale of 3-4 H-bonds [44]
Beta-sheet nanocrystals	Nanometer	Critical beta-sheet crystal size between 1-4 nm allows for robust and shear-dominated deformation, enabled by cooperative action of clusters of H-bonds [15, 17, 25]
Fibrils	Submicrometer	Flaw-tolerance state reached if fibril dimension confined to less than H^* = 50 nm width; enables concerted contribution of massive numbers of beta-sheet nanocrystals across entire fibril length of several micrometers (see Fig. 4a-b for direct visualization; red color=Regime IV) (this study)
Fibers	Micrometer	Bundling of several fibrils into fibers where each fibril is in flaw-tolerance state; akin to concept of structure splitting mechanism [31] where bundles of fibrils are assembled into fibers to enhance the overall mechanical properties (as schematically shown in Fig. 1d, left)
Spider web	Centimeters	Characteristic softening-stiffening nonlinear material behavior of spider silk combined with the discrete structure of the spider web leads to localized failure of webs [45]

Figures and Figure Captions

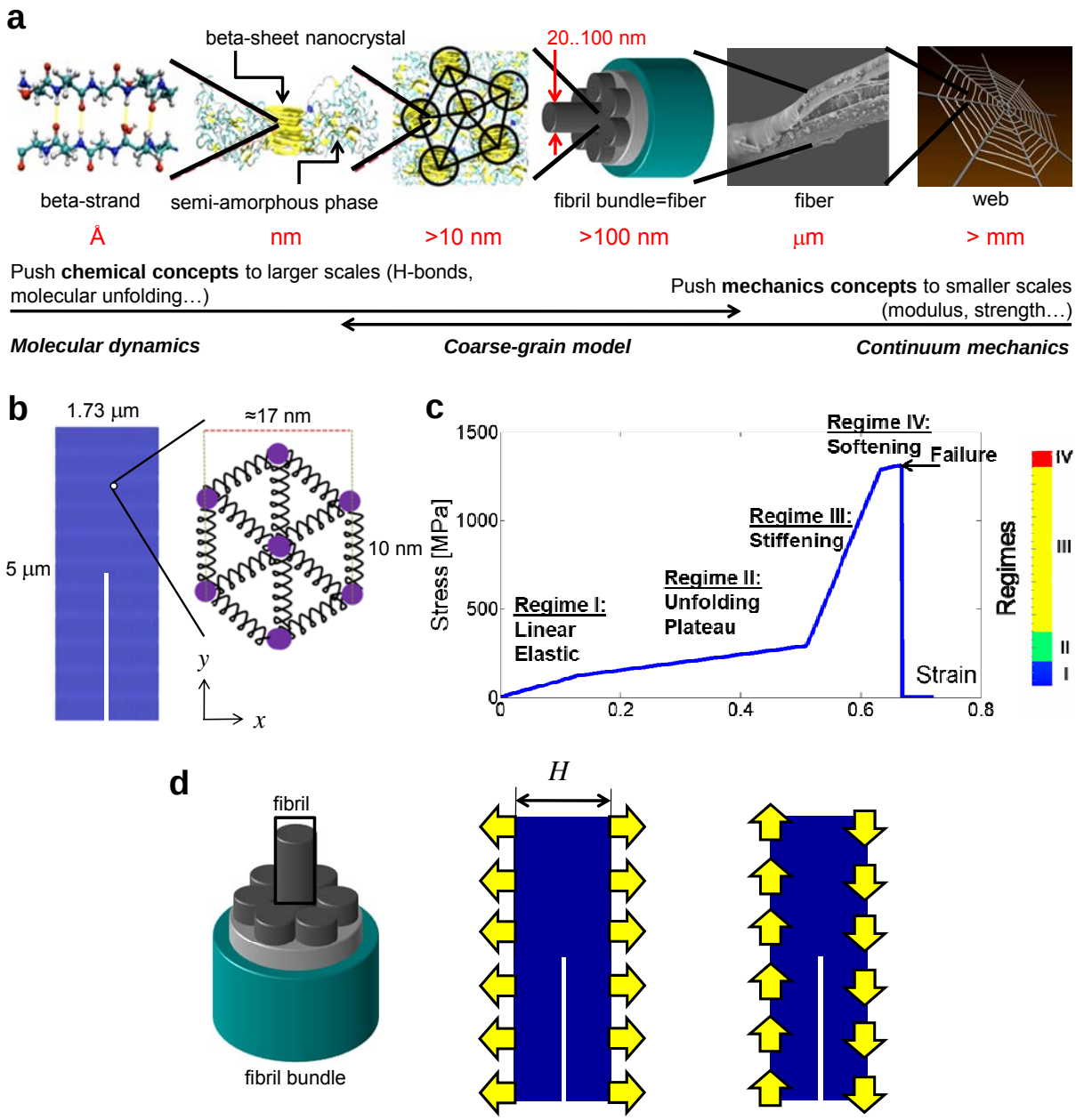

Figure 1 | **Hierarchical levels in spider silk including detailed views of the microscale structure, and formulation of the coarse-grained model**. **a**, Schematic structure of spider silk from nanoscale to macroscale. The image second from right reprinted from reference [46], and the image third from right shows the silk fiber bundle model where silk fibrils are found experimentally to be confined to diameters in the range from 20-100 nm [21, 22, 25, 30]. The coarse-grain model is used here as a tool to push chemical concepts to larger scales, and to push mechanical concepts to smaller scales. **b**, Triangulated mesh of the particle-spring model with similar length-scales to that of the molecular representation seen in panel **a,** where the spacing between particles corresponds to the distance between beta-sheet nanocrystals shown in **a**; used here to model a larger-scale silk fibril with dimensions of several micrometers. **c**, Constitutive stress-strain curve for a triangular unit cell of silk, noting the key transition points between the four regimes marked by molecular events at the molecular scale. The transition from Regime I to Regime II marks the onset of unfolding of the semi-amorphous

phase of silk; the transition from Regime II to Regime III marks the onset of stretching of the beta-sheet nanocrystal phase. In Regime IV beta-sheet nanocrystals begin to fail via a stick-slip mechanism, eventually leading to failure. **d**, Skin-core model of silk fibers consisting of bundles of fibrils (schematic; number of fibrils in a bundle is larger than shown here). The images on the right show the loading geometries used here, implementing tensile (mode I) and shear (mode II) loading.

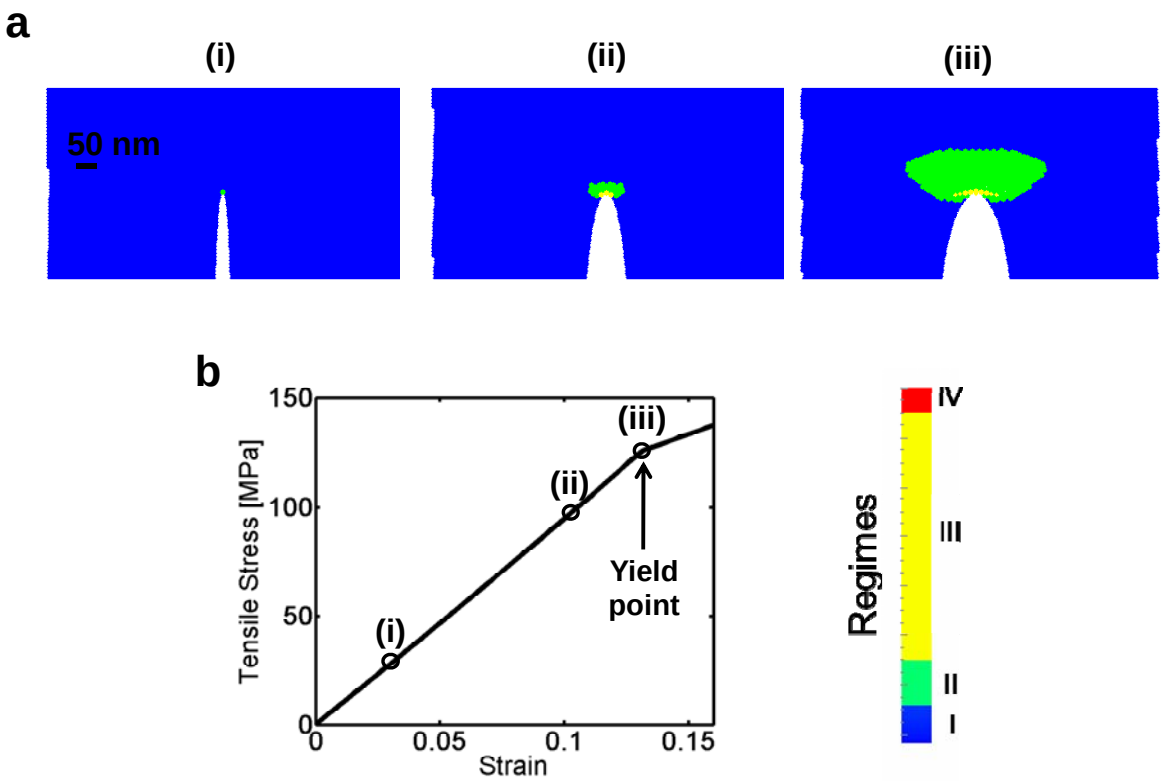

Figure 2 | **Macroscale deformation behavior and evolution of molecular unfolding events close to the crack tip as the applied strain is increased, for a system with a fibril width of 1.73 μm**. **a**, Snapshots of the deformation field as the applied strain is increased, corresponding to the points shown in the stress-strain plot shown in panel **b** (color code for the different deformation regimes shown below panel (iii), corresponding to the regimes shown in Fig. 1c). (i), Deformation field at ≈ 3% applied strain when a small region (confined to ≈ 10 nm length) has entered the unfolding regime. (ii), Deformation field at ≈ 10 % applied strain. (iii), Deformation field at ≈13 % applied strain when macroscale softening occurs as shown in panel **b**, marked as the "yield point". At ≈13 % applied strain the region that has undergone molecular unfolding (Regime II) is confined to a length-scale of ≈ 100 nm, and the region in which beta-sheet nanocrystals are being stretched (Regime III) extends to ≈ 17 nm. **b**, Macroscale stress-strain curve with locations indicated that relate to the snapshots shown in panel **a**. Upon softening the material fails shortly thereafter at 20% strain when the macroscale stress drops to zero. This maximum strain is significantly smaller than observed in experiment where strains of up to 60% are reached (e.g., reference [5]), and where the stress-strain behavior shows a stiffening regime before breaking.

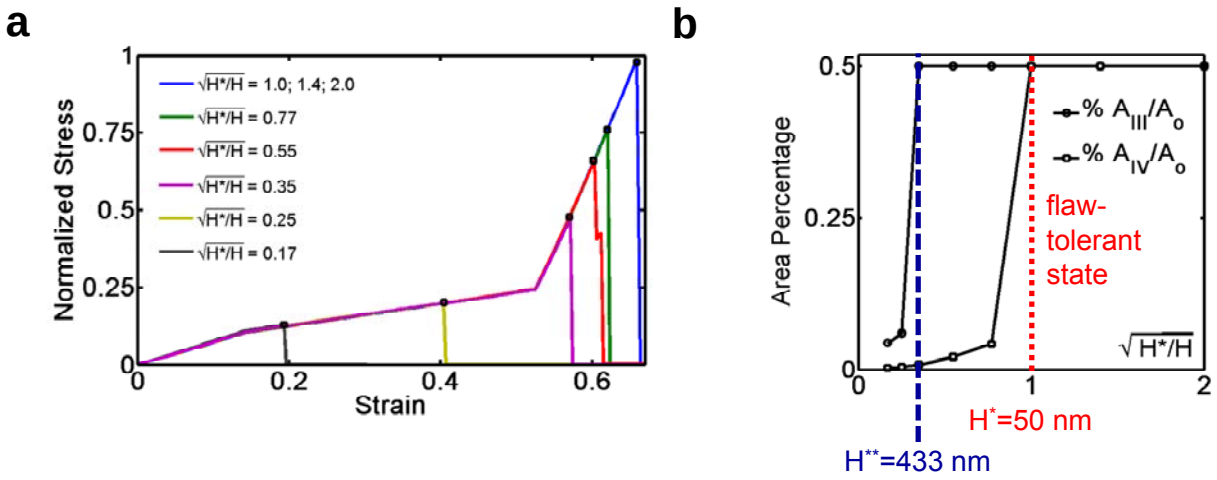

Figure 3 | **Stress-stain curve and strength as a function for different fibril sizes. a**, Normalized stress-strain curves for different slab widths (the stress is normalized by the maximum attainable stress, which is $\sigma_{max}/2$ since the crack extends through half the slab as seen in Fig. 2a. **b**, Percentage of the slab area that has reached Regime III and Regime IV (note the maximum attainable fraction is 50% since the crack extends half way through the slab). The results for Regime IV confirm that below the critical length $H^* = 50$ nm the entire slab contributes to the strength, marking a massive increase at small H compared with the cases for large values of H. The transition point for Regime III occurs already at a slab size of 433 nm, suggesting that below $H^{**} = 433$ nm the entire slab area ahead of the crack has unfolded. However, as can be seen in panel **a** the full potential of the stress-strain curve is not reached since the rupture of the material is governed by only a small percentage of the slab that enters Regime IV.

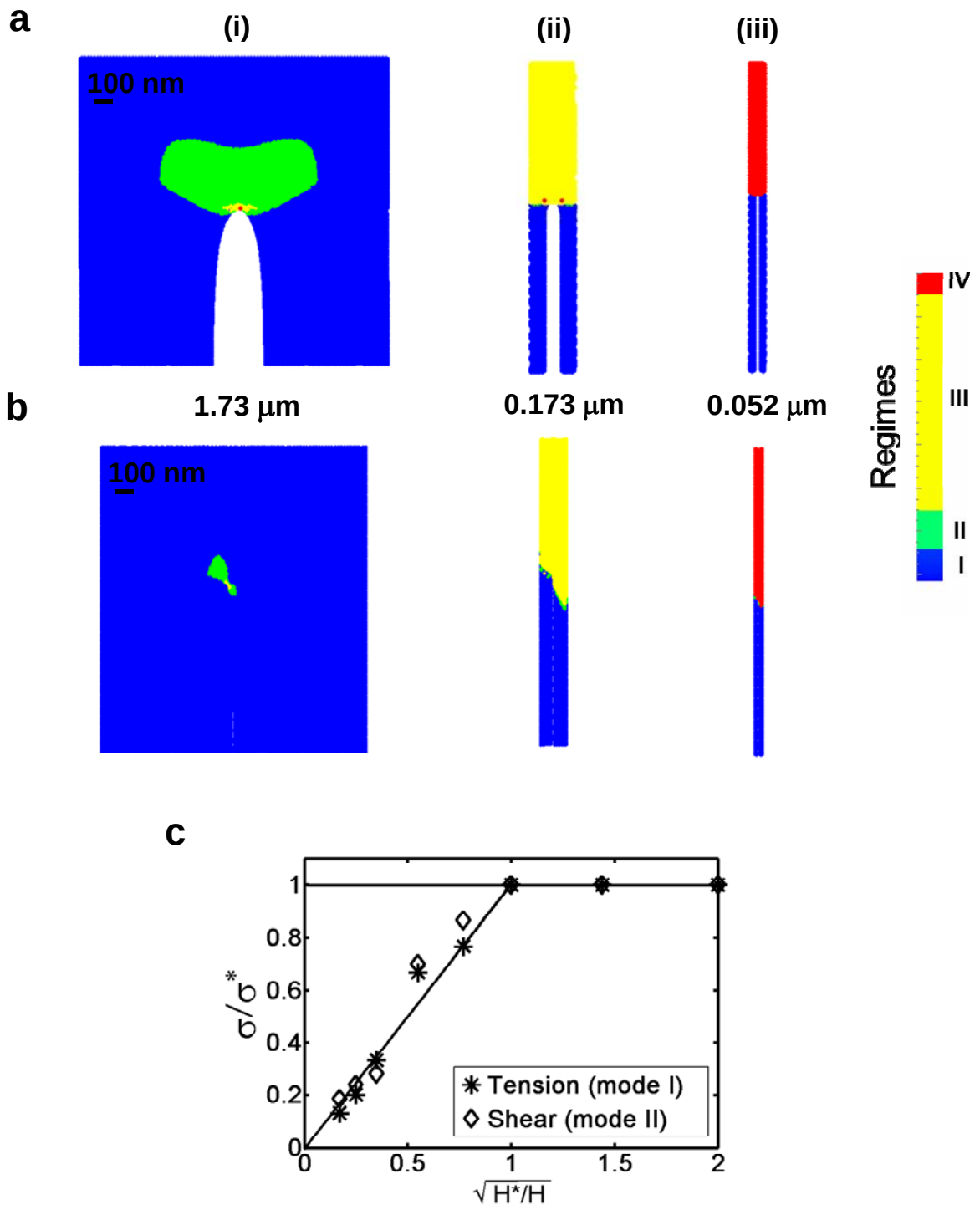

Figure 4 | **Analysis of the failure mechanism as a function of the fibril size *H* under tension (mode I) and shear (mode II)**. **a**, Series of snapshots taken at the failure point of each fibril, for varied slab widths, under tensile (mode I loading). (i), *H*=1.73 μm. The extension of Regime III features a dimension of ≈35 nm; while the region in Regime II has dimensions of ≈285 nm. (ii), *H*=0.173 μm. The stress concentration seen in panel (i) is replaced by a homogeneous deformation state at failure where the entire material ahead of the crack has entered Regime III. (iii), *H*=0.052 μm. The deformation state is not only homogeneous, with almost all particles having entered Regime IV, but failure also occurs also at the failure stress and strain corresponding to a "crack-free" slab, marking a flaw-tolerant state. **b**, Series of snapshots taken at the failure point, for varied slab widths, under

shear (mode II loading). A similar behavior as found in mode I is seen here, where the deformation field becomes increasingly homogeneous as the size is reduced. **c**, Dependence of the normalized failure stress on the normalized slab width for uniaxial tension (mode I) and shear (mode II). The reference values mark the critical length case (H^*≈50 nm) for both loading cases. The data shows that when the slab width is in the range of 50-100 nm, the failure strength approaches the theoretical limit.